

Molecular-Level Analysis of Shock-Wave Physics and Derivation of the Hugoniot Relations for Fused Silica

M. Grujicic, B. Pandurangan, Z. Zhang, W.C. Bell, G.A. Gazonas, P. Patel, and B.A. Cheeseman

(Submitted June 3, 2011)

Equilibrium and non-equilibrium molecular-dynamics simulations are employed in this study to investigate various aspects of shock waves in fused silica (a pure SiO₂ amorphous material used in transparent-armor applications). Equilibrium molecular-dynamics simulations are used first to validate that the initial (unshocked) fused silica possesses the appropriate mass density and microstructure (as characterized by its partial Si-Si, Si-O, and O-O radial distribution functions). Next, non-equilibrium molecular-dynamics simulations are employed, within a continuously contracting computational-cell scheme, to generate planar longitudinal (uniaxial motion) shocks of different strengths. By examining and quantifying the dynamics of shock-wave motion, the respective shock-Hugoniot relations (i.e., functional relations between various material-state variables in the material states produced by the shocks of different strengths) are determined. This methodology suggested that irreversible non-equilibrium deformation/damage processes play an important role in the mechanical response of fused silica to shock loading and that the “equilibrium” procedures for Hugoniot determination based on the equation of state and the Rankine-Hugoniot equation may not be fully justified. Finally, the non-equilibrium molecular-dynamics simulations were used to identify the main microstructure modifying/altering processes accompanying the shock-wave motion through fused silica.

Keywords fused silica, Hugoniots, non-equilibrium molecular-dynamics simulations, shock waves

1. Introduction

Transparent blast/ballistic-impact-resistant vehicle structures (e.g., windshields, door windows, viewports, etc.), employed in ground and air vehicles, utilize a variety of non-glass transparent materials such as transparent crystalline ceramics (e.g., aluminum-oxinitride spinel, AION, sapphire (Ref 1)), and new transparent polymer materials (e.g., transparent nylon (Ref 2)). Despite the well-established benefits offered by these novel transparent materials, ballistic ceramic-based glasses are still important constituent materials in a majority of transparent impact-resistant structures (i.e., transparent armor) used today. The main reasons for the wide usage of ceramic glasses are (a) glass-structure fabrication technologies enable the production of curved, large surface-area, transparent structures with thickness approaching several inches; (b) material processing and product manufacturing are associated with relatively low costs; and (c) ballistic and blast impact survivability of ceramic glasses can be substantially improved through the use of techniques, such as compositional modifications, chemical

strengthening, controlled crystallization, and through the use of various fabrication-process control strategies (Ref 3).

In addition to their good overall blast/ballistic-impact capabilities, some classes of ceramic glasses have been found to exhibit particularly good performance against shaped charge jets. These (molten-metal, high-velocity) jets are produced during impact of warheads consisting of an explosive (located at the back of the warhead and capped at the front by a backward pointing metal liner) and a conical hollow front section (Ref 4). The extremely high explosion-induced pressures cause the forward inversion of the metal liner along the warhead axis, and the accompanying large dissipative plastic work results in the formation of a high-velocity forward traveling jet(s) of molten metal. While the aforementioned finding pertaining to the superior resistance of ceramic glasses to impact by shaped charge jets are believed to be closely related to the glass chemistry and microstructure of these materials, details of the underlying chemistry/microstructure/performance relations are not well understood.

The development of new glass-based, transparent, impact-resistant structures, aimed at reducing the vulnerability of protected-vehicle occupants and on-board instrumentation to various blast/ballistic threats, is nowadays mainly based on the empiricism, legacy knowledge, and the traditional “fabricate-and-test” strategies. While these experimental strategies are very critical for ensuring the reliability and effectiveness of the transparent, impact-resistant structures, they are generally associated with high costs, long lead times and destructive “one-shot” testing. In recent years, these experimental strategies have begun to be increasingly complemented by the corresponding computation-based modeling and simulation efforts. However, it is now well-established (Ref 5–7) that the effectiveness and reliability of the computation-based modeling and simulation approaches are greatly affected by the fidelity of

M. Grujicic, B. Pandurangan, Z. Zhang, and W.C. Bell, Department of Mechanical Engineering, Clemson University, 241 Engineering Innovation Building, Clemson, SC 29634-0921; and **G.A. Gazonas, P. Patel, and B.A. Cheeseman**, Army Research Laboratory-Survivability Materials Branch, Aberdeen Proving Ground, MD 21005-5069. Contact e-mail: gmica@clemson.edu.

Report Documentation Page			Form Approved OMB No. 0704-0188	
<p>Public reporting burden for the collection of information is estimated to average 1 hour per response, including the time for reviewing instructions, searching existing data sources, gathering and maintaining the data needed, and completing and reviewing the collection of information. Send comments regarding this burden estimate or any other aspect of this collection of information, including suggestions for reducing this burden, to Washington Headquarters Services, Directorate for Information Operations and Reports, 1215 Jefferson Davis Highway, Suite 1204, Arlington VA 22202-4302. Respondents should be aware that notwithstanding any other provision of law, no person shall be subject to a penalty for failing to comply with a collection of information if it does not display a currently valid OMB control number.</p>				
1. REPORT DATE JUN 2012	2. REPORT TYPE	3. DATES COVERED 00-00-2012 to 00-00-2012		
Molecular-Level Analysis of Shock-Wave Physics and Derivation of the Hugoniot Relations for Fused Silica			5a. CONTRACT NUMBER	
			5b. GRANT NUMBER	
			5c. PROGRAM ELEMENT NUMBER	
6. AUTHOR(S)			5d. PROJECT NUMBER	
			5e. TASK NUMBER	
			5f. WORK UNIT NUMBER	
7. PERFORMING ORGANIZATION NAME(S) AND ADDRESS(ES) Clemson University, Department of Mechanical Engineering, 241 Engineering Innovation Building, Clemson, SC, 29634			8. PERFORMING ORGANIZATION REPORT NUMBER	
9. SPONSORING/MONITORING AGENCY NAME(S) AND ADDRESS(ES)			10. SPONSOR/MONITOR'S ACRONYM(S)	
			11. SPONSOR/MONITOR'S REPORT NUMBER(S)	
12. DISTRIBUTION/AVAILABILITY STATEMENT Approved for public release; distribution unlimited				
13. SUPPLEMENTARY NOTES				
14. ABSTRACT				
15. SUBJECT TERMS				
16. SECURITY CLASSIFICATION OF:			17. LIMITATION OF ABSTRACT Same as Report (SAR)	18. NUMBER OF PAGES 14
a. REPORT unclassified	b. ABSTRACT unclassified	c. THIS PAGE unclassified		

the employed material models (mathematical relations employed to represent interdependencies among various material state variables). In the case of transparent protection systems under investigation in this study, it is critical that these models realistically describe deformation/fracture response of the subject material (ballistic (fused silica-based) glass, in the present case) under high-rate, large-strain, and high-pressure loading conditions encountered during blast/ballistic impact. Therefore, one of the main objectives of the present study is to further advance the application of computational modeling/simulation-based engineering approaches of transparent impact-resistant structures via the potential improvements in fidelity of the associated material (fused silica) models (which, in turn, will be achieved via identification and quantification of processes and phenomena occurring in fused silica under such conditions. Specifically, phenomena and processes associated with the formation and propagation of shock-waves within fused silica will be investigated.

A comprehensive literature review carried out as part of our prior studies (Ref 8, 9) revealed that the mechanical behavior of glass has been modeled predominantly using three distinct approaches: (a) molecular-modeling methods (Ref 8–14); (b) continuum-material approximations (Ref 5–7, 15–18); and (c) meso-length scale models based on explicit representation of cracks (Ref 19, 20). Since a detailed overview of these models can be found in Ref 8 and 9, they will not be discussed any further in the present article. However, it is worth mentioning that the overviews presented in Ref 8 and 9 clearly established that (a) molecular-level models are critical for identifying nanometer length-scale phenomena and the associated microstructure evolution processes accompanying shock-wave propagation and damage/failure evolution; (b) continuum-level models are the only ones which enable large-scale computational analyses of the mechanical response of full-scale transparent-armor protective structures to various blast and ballistic threats; and (c) the models based on explicit representation of cracks and their propagation are mainly suitable for the study of the local deformation and fracture response of simple-geometry test coupons.

Ceramic glasses (like fused silica, investigated in the present study) are amorphous materials. The molecular-level microstructure of these materials involves entities, such as a random network of covalently bonded atoms, atomic free volumes, (network-former) bridging and non-bridging oxygen atoms, cations of glass-modifier species, etc. Despite the absence of a crystalline structure, the microstructure of ceramic glasses is not completely random but rather involves different extents of short- and intermediate-range order, spanning over a range of length-scales (from the quantum-mechanical to the continuum-level). That is the reason that as a part of this larger research effort, involving the scientists from the Army Research Laboratory, Aberdeen Proving Ground, MD and Clemson University, a multi length-scale modeling and simulation approaches have been adopted in the investigation of various ceramic glasses.

A schematic of the adopted multi-length-scale approach is depicted in Fig. 1 in which the characteristic length-range is shown along the abscissa, and the characteristic time-scale is shown along the ordinate for the following selected length-scales: (a) electronic scale: within which the material is investigated using quantum-mechanical methods and tools; (b) atomic/molecular length-scale—within which molecular-statics and -dynamics computational techniques are employed;

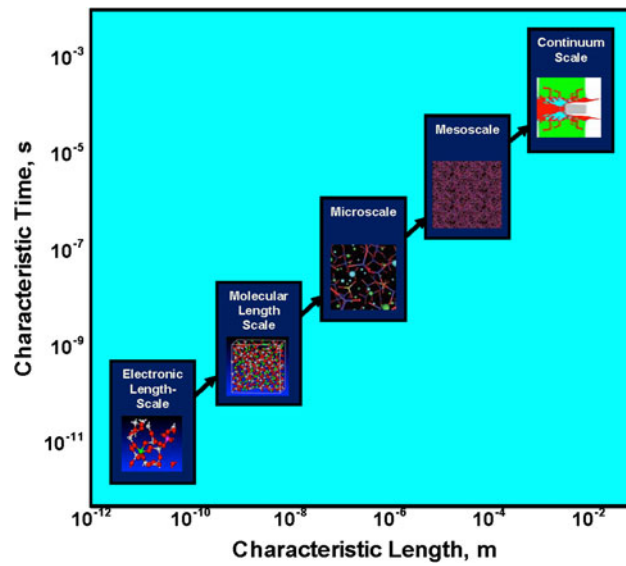


Fig. 1 A schematic of the multi-scale modeling and simulation approach utilized in our ongoing study on ceramic glasses

(c) micro length-scale—within which various aspects of the short-range order are investigated using Monte Carlo-based stochastic methods; (d) meso length-scale—within which the role of intermediate-range order and long-range disorder is analyzed using various network-dynamics computational schemes; and (e) continuum length-scale—within which the contribution of all the finer length-scales is incorporated into the appropriate homogenized/smeared-out material model, and subsequently used within finite element-based transient nonlinear dynamics computational methods and tools. While all the aforementioned length-scales are being investigated in our ongoing research and several classes/grades of ceramic glasses are being analyzed, the present article deals only with the molecular-level length-scale and with fused silica.

As mentioned above, within the present study, molecular-level computational methods are employed to investigate shock-wave-related phenomena in fused silica. A shock wave (or shock for short) is a wave which propagates through a medium at a speed higher than the sound speed, and its passage causes an abrupt (discontinuity-like) change in the material state variables (e.g., pressure/stress, internal energy density, mass-density, temperature, and particle velocity). Shocks of higher strength give rise to larger extents of state-variable changes and propagate at higher speeds. Furthermore, unlike the acoustic waves which produce isentropic (constant entropy) changes in the material state, shocks bring about irreversible (entropy-increasing/energy-dissipating) material-state changes. In fluids, energy dissipation is mainly caused by high-rate viscous damping phenomena, while in solids, inelastic deformation processes play a key role in the irreversibility of material-state changes and in energy dissipation associated with shock loading.

In our recent study (Ref 9, 21), molecular-level computational methods and tools were used to investigate shock-related phenomena in soda-lime glass and polyurea. The key findings obtained in these studies can be summarized as follows: (a) propagation of a disturbance caused by (impulsive) external loading typically results in the formation of steady (time-invariant structured) shocks, and this process is facilitated by

the operation of intrinsic rate-dependent energy-dissipative mechanisms. However, unlike fluids in which shock-induced energy dissipation is mainly related to viscous damping, in solids, the dominant energy-dissipation mechanisms are associated with various inelastic-deformation/damage processes resulting from concerted lateral slippage of the particles; (b) in the case of soda-lime glass, the inelastic-deformation processes involve chemical-bond breaking, ring-size modifications, and atomic coordination/network structure changes. In the case of (segmented and micro-segregated) polyurea, on the other hand, these processes were mainly related to the degradation and breakage of the hydrogen bonds within the so-called hard-segments; and (c) in order to eliminate free-surface effects, molecular-level modeling of shocks had to be carried out using computational systems with periodic boundary conditions (at least in the directions transverse to the shock-wave propagation direction). To attain steady-wave conditions of the shock, computational domains sufficiently long in the direction of shock-wave propagation had to be employed. Furthermore, lateral dimensions of the computational domain had to be also sufficiently large to avoid spurious effects associated with the use of the periodic boundary conditions. Consequently, computational domains involving several tens of thousands of atoms had to be employed. The corresponding computational times (controlled by the shock-wave travel time) were of the order of 5-20 ps. This limited the shock thicknesses to around 10 nm and the corresponding rise times to ca. 0.5-1 ps. Thus, weak shocks with thicknesses of hundreds of nanometers could not be analyzed using molecular-level methods (at least in their steady-wave regime).

While recognizing the aforementioned aspects and potential limitations of molecular-level modeling of shock, the present study addresses the problem of shock generation/propagation in fused silica and has the following two main objectives:

- (a) Determination of the shock Hugoniot relations (centered on the initial stress-free quiescent state) in fused silica. Hugoniot is the (stress versus specific volume versus energy density versus temperature versus entropy density versus particle velocity versus shock speed) locus of the material states generated by the passage of shocks of various strengths. It is most often used (i) in the derivation of the continuum-level high-loading rate material models (particularly in the derivation of the equation of state); and (ii) in the analysis of planar-shock dynamics and various shock reflection/interaction phenomena and
- (b) Characterization and quantification of the material state and the microstructure-altering processes resulting from the passage of shocks of various strengths. Among these processes are those which involve reversible and irreversible densifications, chemical-bond breaking, coordination-number modifications, ring-size alterations, and other manifestations of the changes to the short- and intermediate-range orders. Such changes have been observed even under quasi-static loading conditions such as those encountered during simple Hertzian indentation testing (Ref 3).

The organization of the article is as follows: A brief overview of the random-network model for microstructure of amorphous materials and its application to fused silica are provided in section 2. The molecular-level modeling and simulation procedure employed is presented in great detail

in section 3. Key results pertaining to validation of the room-temperature density and microstructure of fused-silica, dynamics of planar, longitudinal shock-wave motion, and shock-Hugoniot relations are presented and discussed in section 4. A summary of the main findings and conclusions is provided in section 5.

2. Molecular-Level Microstructure of Fused Silica

As mentioned earlier, one of the basic properties of ceramic glasses (or of glasses, in general) is their lack of long-range atomic order which places them into a class of amorphous materials. For instance, the atomic arrangement in pure silicate glass (i.e., fused silica) is highly random relative to the chemically equivalent (crystalline) quartz. To describe the structure of ceramic glasses as determined using various experimental techniques (e.g., neutron-diffraction, nuclear magnetic resonance, small angle X-ray scattering (SAXS), etc.), the so-called random network model (Ref 22) is typically employed. Such a model represents amorphous materials as a three-dimensional-linked network of polyhedra. The character (number of facets) of the polyhedra is controlled by the species-specific coordination of the central (glass-forming) atom (cation). In the case of silicate-based glasses, like fused silica and soda-lime glass, the polyhedron-center atoms are all silicon, and each silicon atom is surrounded by four oxygen atoms (while each oxygen atom is connected to or bridges two silicon atoms) forming a SiO_4^{4-} tetrahedron. In glasses of different formulations, other types of polyhedra may exist. Since silicon has a tendency to form a continuous network with (bridging) oxygen atoms, SiO_2 is commonly referred to as a “network former.” Other potential network formers in glass are boron and germanium oxides.

Numerous oxides and other additives are utilized to modify the basic silica tetrahedra network of silicate-based glasses to tailor their properties to specific applications. When alkali (or alkaline earth) oxides are added to a pure silicate-based glass, to accommodate the excess of oxygen anions which are present due to the oxide dissociation, the continuity of the silica tetrahedra network becomes disrupted. The resulting glass structure contains additional non-bridging (connected to only one silicon atom) oxygen atoms. Charge transfer from the alkali earth metal atoms converts the non-bridging oxygen atoms into singly charged anions. The metallic cations formed in this process tend to hover around the non-bridging oxygen ions for local charge neutrality. Since alkali (or alkaline earth)-based oxides cause a disruption in the continuous glass network, they are typically referred to as “network modifiers.” As mentioned earlier, fused-silica ceramic glass investigated in the present study is chemically pure SiO_2 (i.e., free of glass modifiers) and contains a continuous network of Si-O bonds (i.e., it is free of non-bridging oxygen atoms).

Within the random network model, the microstructure of glass is described using several network state parameters. Among these, the most frequently used are (a) the so-called R parameter, defined as the average number of oxygen ions per network-forming ion which describes the overall connectivity of a given network. In the case of fused silica, in which there are two (bridging) oxygen anions for every network-forming silicon cation, the R value is 2.0. In general, a larger value of the R parameter (brought about by the addition of network

modifiers) implies a more open (less connected) weaker amorphous glass network. The effect of network formers on the R parameter is more complicated and depends on the network former coordination number, the strength of its bond with oxygen as well as its concentration; (b) the so-called X parameter which defines the average number of non-bridging (connected to only a single network-forming cation) oxygen atoms per network polyhedron and takes on a zero value in the case of fused silica and; (c) the so-called Y parameter which defines the average number of bridging (connected to two network-forming cations) oxygen atoms per network polyhedron and takes on a value of 4.0 in the case of fused silica.

In addition to the three parameters mentioned above, the “seemingly” random microstructure of ceramic glasses is also described using bond-length, bond-angle, pair-wise correlation, Voronoi-cell volume, etc. distribution functions. A more detailed description of these microstructural parameters will be provided in section 4, as part of a discussion of the results pertaining to the structure of the as-shocked fused silica.

3. Molecular-Level Analysis of Fused silica

As mentioned earlier, molecular-level computational methods have been employed in the present study to investigate various shock-wave-related phenomena in fused silica. Within these methods, all atoms and bonds are explicitly accounted for and molecular mechanics and dynamics algorithms are employed to quantify the state and behavior of the material under investigation. Molecular-level simulation problems typically require the specification of the following: (a) a molecular-level computational model consisting of atoms, ions, functional groups, and/or molecules; (b) a set of force field functions; and (c) computational method(s) to be used in the simulation. More details of these three aspects of the molecular-level modeling and simulation of fused silica are provided later.

3.1 Computational Model

At the molecular level, fused silica is modeled as a discrete-particle-based material consisting of silicon (Si) and oxygen (O) atoms mutually bonded via a single covalent bond and forming a connected, non-structured/amorphous network of silica (SiO_4^{4-}) tetrahedra.

While fused silica is an amorphous material and does not possess any long-range regularity in its atomic/molecular structure, modeling of bulk behavior of fused silica is typically done at the molecular level by assuming the existence of a larger (amorphous) unit cell. Repetition of this cell in the three orthogonal directions (the process also known as application of the “periodic boundary conditions”) results in the formation of an infinitely large bulk-type material. This procedure has been adopted in the present study.

The parallelepiped-shaped computational cell used in the present (shock-wave) analysis contained 4608 particles (1536 Si atoms and 3072 O atoms). The edge-lengths of the computational cell were initially set to $a = 10.36$ nm and $b = c = 2.59$ nm, yielding a fused silica’s initial nominal density of 2.2 g/cm^3 . The three edges (a , b , and c) of the cell were aligned, respectively, with the three coordinate axes (x , y , and z).

To create the ambient temperature/pressure equilibrium atomic configuration within the computational cell, the following procedure was implemented within the Visualizer (Ref 23)

program from Accelrys: (a) a starting computational cell was first constructed by stacking the appropriate number of fused silica unit cells in the three orthogonal directions. This was followed by the affine distortion of the computational cell to obtain the correct dimensions and density of the computational cell; (b) a stochastic bond-switching algorithm was then implemented (Ref 24) within a Monte Carlo computational procedure to convert the crystalline structure into a disordered structure. Within this algorithm, two neighboring Si-O pairs were randomly selected from the computational cell, and the energy ΔE resulting from the Si-O bond switching was computed. In the $\Delta E < 0$ case, the bond switching in question was accepted without any additional condition. On the contrary, in the $\Delta E > 0$ case, a Boltzmann probability factor, $P_B = \exp(-\Delta E/(3NkT/2))$ (where k is the Boltzmann’s constant), was first calculated and compared with a random number RN drawn from a (0,1) uniform distribution function. The bond switching in question was then adopted only if $P_B > RN$; (c) the resulting structure was then subjected to a carefully devised set of NVT (where $N(=4608)$ is the (fixed) number of atoms within the computational cell, V , the computational cell volume (also fixed), and T is a fixed temperature) molecular-dynamics simulations. Specifically, the NVT simulations were started at a temperature of 5300 K and carried out in such a way that the temperature was controlled using the following “simulated-annealing” scheme: (i) a particle-velocity scaling algorithm was applied to every time step for the first 6000 steps. This enforced strict control of the temperature but produced particle velocities which were inconsistent with the target-temperature Maxwell-Boltzmann distribution function; (ii) within the next 6000 NVT simulation steps, the frequency of particle-velocity scaling was decreased to every 40 time steps while a Nose-Hoover (Ref 25) temperature control algorithm (“thermostat”) was applied between the particle-velocity scaling steps. A brief description of the Nose-Hoover thermostat is provided in Appendix A; and (iii) during the final 8000 steps, the temperature was controlled using only the Nose-Hoover thermostat. This procedure ensured an efficient temperature control while yielding an equilibrium state of the material (i.e., a particle-velocity distribution consistent with the target-temperature Maxwell-Boltzmann distribution function).

Upon establishing the thermodynamic equilibrium at 5300 K, the target temperature was reduced by 500 K, and then this procedure was re-applied at progressively (by 500 K) lower temperatures, until the final temperature of 300 K was reached. The total system equilibration procedure typically involved simulation times on the order of 500 ps resulting in an average cooling-rate of $\sim 10 \text{ K/ps}$. An example of a typical molecular-level topology within a computational cell is displayed in Fig. 2(a). A close-up of the molecular-level random-network is displayed in Fig. 2(b).

3.2 Force Fields

The behavior of a material system at the molecular-level is governed by the appropriate force fields which describe, in an approximate manner, the various interactions taking place between the constituent particles, atoms, ions, charge groups, etc. In other words, the knowledge of force fields enables determination of the potential energy of a system in a given configuration. In addition, gradients of the force-field functions quantify the net forces experienced by the particles, the information that is needed in the molecular-dynamics simulations.

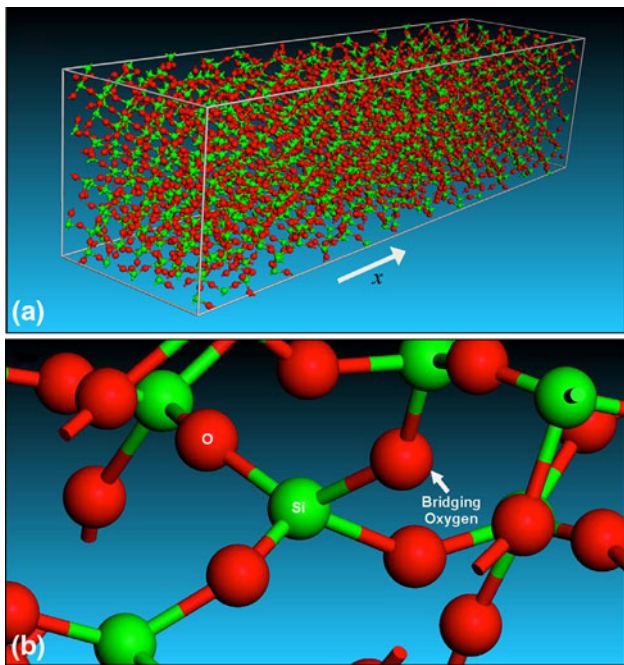


Fig. 2 (a) The computational unit cell for fused silica molecular-level simulations used in the present study and (b) an example of the local atomic structure

In general, the potential energy of a system of interacting particles can be expressed as a sum of the valence (or bond), E_{valence} , cross-term, $E_{\text{cross-term}}$, and non-bond, $E_{\text{non-bond}}$, interaction energies as

$$E_{\text{total}} = E_{\text{valence}} + E_{\text{cross-term}} + E_{\text{non-bond}} \quad (\text{Eq } 1)$$

The valence energy generally accounts for the contribution of valence electrons bonding and contains the following components: (a) a bond length/stretching term; (b) a two-bond angle term; (c) a three-bond dihedral/torsion angle term; (d) an inversion (or a four-atom out-of-plane interaction) term; and (e) the so-called three-atom Urey-Bradley term.

The cross-term interacting energy accounts for the cross-interactions between the aforementioned valence-energy components and includes terms like (a) stretch-stretch interactions between two adjacent bonds; (b) stretch-bend interactions between a two-bond angle and one of its bonds; (c) bend-bend interactions between two valence angles associated with a common vertex atom; (d) stretch-torsion interactions between a dihedral angle and one of its end bonds; (e) stretch-torsion interactions between a dihedral angle and its middle bond; (f) bend-torsion interactions between a dihedral angle and one of its valence angles; and (g) bend-bend-torsion interactions between a dihedral angle and its two valence angles.

The non-bond-interaction term accounts for the interactions between non-bonded atoms and includes the van der Waals energy and the Coulomb electrostatic energy.

In the present study, the so-called COMPASS (Condensed-phase Optimized Molecular Potentials for Atomistic Simulation Studies) force field is used (Ref 26, 27). This highly accurate force field is of an ab-initio type since most of its parameters were determined by matching the predictions made by the ab-initio quantum mechanics calculations to the condensed-matter experimental data. A summary of the COMPASS force-field functions can be found in our previous study (Ref 28).

3.3 Computational Method(s)

All the molecular-level (i.e., equilibrium and non-equilibrium molecular dynamics) calculations were carried out within the present study using Discover (Ref 29) (an atomic simulation program from Accelrys).

Within the equilibrium molecular-dynamics method, the system under consideration is coupled to an (external) environment (e.g., constant-pressure piston, constant-temperature reservoir, etc.) which ensures that the system remains in equilibrium (i.e., the system is not subjected to any thermodynamic fluxes). In the present study, *NVT*, *NPT* (*P* is pressure), and *NVE* (*E* is the total energy) equilibrium molecular-dynamics simulations were used. Equilibrium molecular-dynamics calculations enable determination of the (equilibrium) thermodynamic properties of a material system through the use of time averages of the state variables sampled along the calculated system trajectories.

Within non-equilibrium molecular dynamics, the system is subjected to large perturbations which create a thermodynamic flux (e.g., the flux of energy and momentum).

3.4 Generation of Planar Shock-Waves

To generate a planar shock (or more precisely a pair of planar shocks) within the thermodynamically equilibrated material system (discussed earlier), the computational cell was continuously contracted along the axial *x*-direction. This was accomplished by varying/reducing the lattice parameter *a* as

$$a(t) = a(t=0) - 2u_p t \quad (\text{Eq } 2)$$

where *t* denotes time, u_p is the so-called piston velocity (or equivalently the particles upstream/behind-the-shock velocity) in the *x*-direction. u_p is varied over a range between 250 and 3250 m/s to simulate the generation and propagation of shock of various strengths. Meanwhile, computational-cell transverse lattice parameters *b* and *c* are kept constant to obtain planar (uniaxial-strain) shock conditions. In this process, the computational cell faces normal to the shock propagation-direction behave very similarly to the impact-surface of a plate-like target subjected to a so-called symmetric “flyer-plate” impact test (Ref 30). Owing to the use of the periodic boundary conditions in the computational cell contraction direction, the procedure employed here generates a pair of planar longitudinal shocks which propagate at a shock speed U_s from the computational cell faces (normal to the computational cell contraction direction) towards the cell center. As schematically shown in Fig. 3, these shocks leave behind a “shocked” material state characterized by a higher material density (as well as by higher levels of internal energy, temperature, stress, particle velocity, and entropy).

3.5 Problem Formulation

The problem addressed in the present study involved generation of shocks of different strengths (using the aforementioned computational cell parameter contraction method), determination of the associated shock-Hugoniot relations and identification and elucidation of the main molecular-level inelastic-deformation/energy dissipation processes taking place at or in the vicinity of the shock front. The procedure for shock-wave generation was presented in the previous section and will not be considered any further.

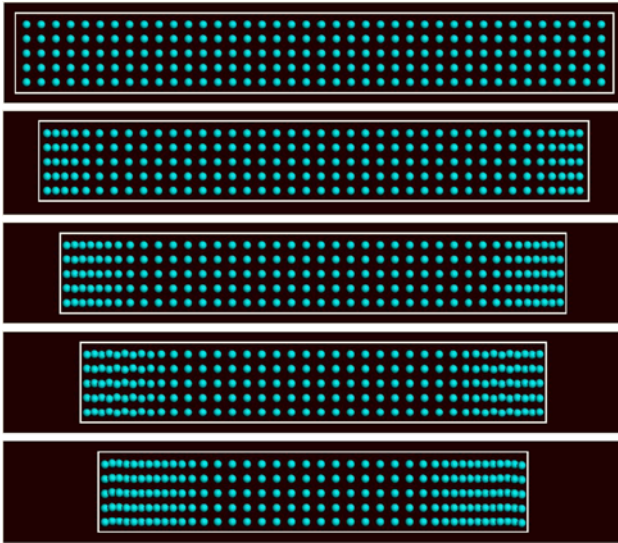


Fig. 3 A schematic of the generation of a pair of shocks in a molecular-level system via the process of computational-cell parameter contraction

As far as the shock Hugoniot determination is concerned, it entailed the knowledge of the shock-wave profiles (and their temporal evolution) for the axial stress, material density, particle velocity, internal energy and temperature. The latter are obtained by lumping particles/atoms and their (bond and non-bond) potential and kinetic energy contribution, into fixed-width bins, in the order of their axial coordinates. As will be shown in the next section, two types of bins are used: (a) a Lagrangian-type which is fixed to the initial/reference state of the computational cell and (b) a moving-type which is attached to the advancing shock front.

Identification of the molecular-level inelastic-deformation/energy dissipation processes entailed a close examination of the changes in a material bond structure and topology caused by the passage of the shock.

4. Results and Discussion

4.1 Validation of the Computed Equilibrium Material State

In this section, an attempt is made to validate the fused silica room temperature/ambient pressure equilibrium structure obtained through application of the previously described simulated-annealing computational procedure. In particular, the material density, partial radial distribution functions for the three (Si-Si, Si-O, and O-O) atomic pairs and the (equilibrium) negative axial-stress versus specific volume shock-Hugoniot relation are calculated and compared with their experimental counterparts.

To compute the material density and the partial radial distribution functions, *NPT* equilibrium molecular dynamic simulations were run at the room temperature and the ambient pressure. Simulations were carried out for over 6000 (0.1 fs) time steps, while maintaining the temperature using the Nose-Hoover thermostat and scaling the particle velocities for every ten time steps. Pressure was controlled using a Berendsen barostat (Ref 31). A brief overview of this barostat is provided in Appendix B. To obtain the equilibrium Hugoniot relations, a series of *NVT*

simulations (described below) were carried out. Each simulation was run for over 6000 (0.1 fs) time steps, while the temperature was controlled using the Nose-Hoover thermostat.

4.1.1 Density. The average mass-density of fused silica computed from the computational cell average volume and the cell mass has been found to be 1.5-2.0% greater than the target density of 2.2 g/cm³. This computation/experiment agreement has been deemed to be fair.

4.1.2 Radial Distribution Functions. The partial radial-distribution (often also referred to as the partial pair-correlation) function provides a measure of the probability that, given the presence of an atom of type α at the origin of an arbitrary reference frame, there will be an atom of type β within a spherical shell of infinitesimal thickness dr at a distance r from the reference atom. In amorphous materials like fused silica, the partial pair-correlation functions are quite important since they (a) provide an insight into the short-range order of the system; (b) can be used in the assessment of continuum-level thermodynamic material properties; and (c) provide a way of validating the molecular-level calculations since these quantities can be determined experimentally using X-ray diffraction.

The computed partial radial-distribution functions are compared with their counterparts based on the shell model molecular-dynamics calculations (Ref 32). The results of this comparison are displayed in Fig. 4(a) and (b). Careful examination of the present results displayed in Fig. 4(a) shows that they are qualitatively similar to the ones reported in Ref 32. As far as the quantitative agreement between the two sets of results is concerned, it could be characterized as being fair.

4.1.3 Negative Axial-Stress versus Specific Volume Equilibrium Shock Hugoniot. Finally, the method of Erpenbeck (Ref 33) is employed to compute the “equilibrium” negative axial-stress versus specific volume Hugoniot relations for fused silica. Toward that end, a Rankine-Hugoniot function is first constructed as

$$H(T, V) = E(T, V) - E_0(T_0, V_0) + \frac{1}{2}(-t_{11}(T, V) + -t_{11,0}(T, V))(V - V_0) \quad (\text{Eq } 3)$$

where t_{11} denotes the axial stress, and the subscript “0” denotes the initial (unshocked) material state. In order to compute a single point of the negative axial-stress versus specific volume Hugoniot, a series of *NVT* equilibrium molecular-dynamics simulations was carried out. In each of these series of simulations, the computational-cell volume was kept constant while the temperature was varied between different simulations within the same series. Each simulation within a given (fixed volume) series yielded the associated negative axial stress and energy density values. These were next used to evaluate the Rankine-Hugoniot function, Eq 3 at each simulation temperature. Then the value of the temperature at which the Rankine-Hugoniot function is equal to zero is determined via interpolation. Finally, an *NVT* run is carried out at this temperature to determine the corresponding negative axial-stress (and energy density). This procedure is then repeated for a set of (fixed) computational cell volumes, to construct the negative axial-stress versus specific volume Hugoniot (complete) relation. The $-t_{11}$ versus v/v_0 Hugoniot, obtained using the procedure described above, is depicted in Fig. 5. For comparison, the corresponding Hugoniot curve obtained experimentally in Ref 34 is also shown in this figure.

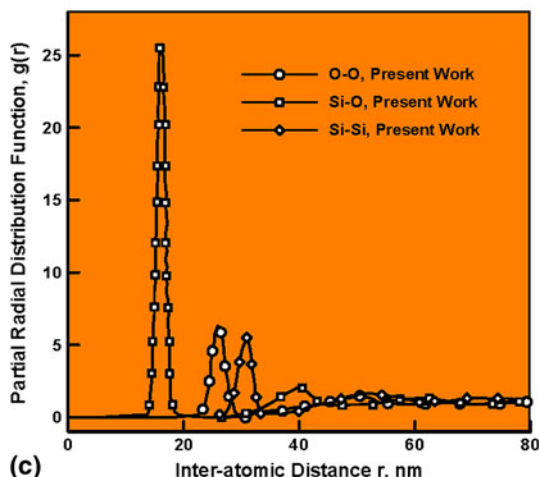
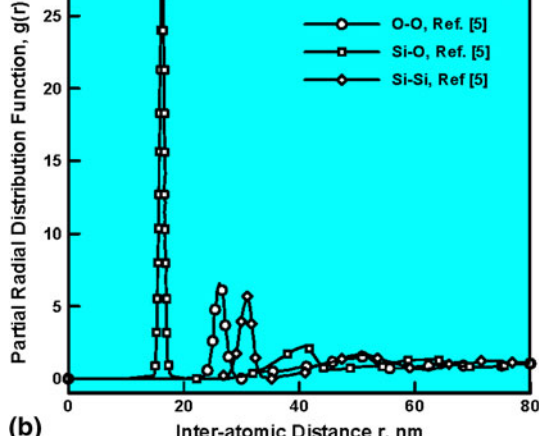
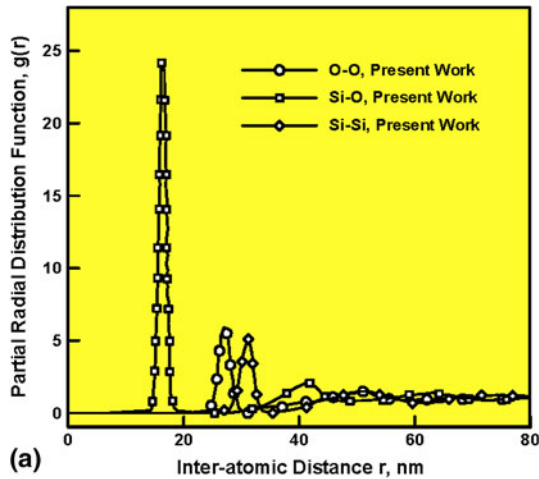


Fig. 4 A comparison between the fused silica Si-Si, Si-O, O-O partial radial-distribution functions computed in (a) the initial equilibrium state, as computed in the present study; (b) the equilibrium initial state as reported in Tilocca et al. (Ref 32); and (c) the as-shocked material state, as computed in the present study

A comparison between the computed and the experimental (Ref 3) Hugoniot curves displayed in Fig. 5 shows that the agreement is relatively good at small compression levels (the weak shock regime) and it worsens as the shock strength is increased (i.e., v/v_0 is decreased). Specifically, at the lowest

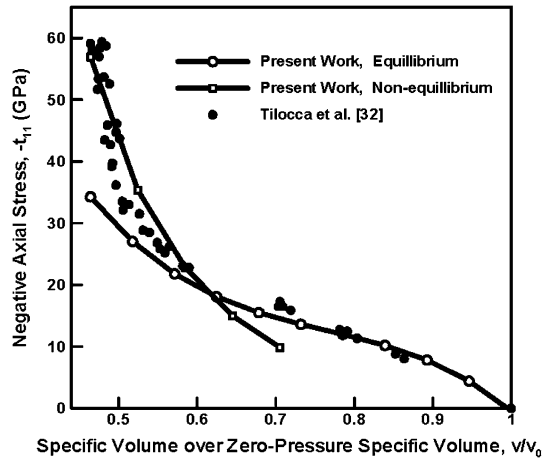


Fig. 5 A comparison between the computed equilibrium, the computed non-equilibrium and the experimentally measured (Ref 3) negative axial-stress versus normalized specific volume Hugoniot curves in fused silica

values of v/v_0 , the negative axial stress is under-predicted by 35–40%.

It should be noted that the Hugoniot relations obtained in this portion of the work are referred to as being of the “equilibrium” character. This was done to emphasize the fact that these relations were obtained using equilibrium molecular-dynamics simulation results. In other words, the determination of the Hugoniot relations was carried out under the assumption that shock loading transitions the initial ambient-pressure equilibrium material state into another, high-pressure, equilibrium material state, (i.e., the dissipative portion of the internal energy change accompanying the passage of a shock is purely thermal). However, shock loading is not only an intrinsically irreversible non-equilibrium energy-dissipating process, but may also, in the case of solid materials, be accompanied by various microstructure-altering processes (e.g., extensive inelastic deformations, damage, phase transformations, etc.). The operation of such processes would cause the as-shocked material state not to lie any longer on the equilibrium equation-of-state surface and, hence, one may question the validity of the equilibrium Hugoniot relations (particularly in the regime associated with intermediate and strong-shocks (the regime in which the equilibrium Hugoniot relations are found not to agree well with their experimental counterparts, Fig. 5)). To test the validity of these relations, non-equilibrium molecular-dynamics simulations are used to generate and drive planar shocks in fused silica. This provided an alternative, more-direct way for determination of the shock-Hugoniot relations. Detailed results related to this portion of the study are presented in the remainder of the article.

4.2 Shock-Wave Molecular-Level Analysis

As explained earlier, the computational cell contraction procedure yielded a pair of converging shocks per computational cell (due to the use of the periodic boundary conditions). Since the two shocks were structurally identical and the collision of the two converging shocks is beyond the scope of the present study, the analysis presented in this and the subsequent sections focus on the behavior of the right propagating shock only.

4.2.1 Identification of the Shock-Wave Front. Figures 6(a) and (b) show examples of the typical results obtained in this portion of the study. These results pertain to material molecular-level microstructure/topology evolution accompanying the propagation of a pair of approaching shocks. Arrows are used in Fig. 6(a) and (b) to indicate an approximate location of the mid-plane of the shock front. The shock front was determined as the region within which a rapid change in the material density is detected. A careful examination of the results displayed in these figures shows that the shock remains fairly planar during its motion. Clearly, this finding was influenced by the fairly limited computational-cell size in the lateral direction as well as by the imposition of the periodic boundary conditions.

4.2.2 Shock-Wave Front Analysis. To obtain a more quantitative description of the shock-wave form, a set of previously described parallel Lagrangian bins stacked in the shockwave propagation direction was utilized. As explained earlier, these bins are fixed to the reference frame of the material and, hence, contain the same set of atoms throughout the simulation. This enables the monitoring of the average properties of fixed sets of atoms to reveal the structure of the advancing shock.

Figure 7(a) and (b) display the results obtained through the use of the aforementioned method in which x -component (i.e., shock propagation direction) particle velocities at different

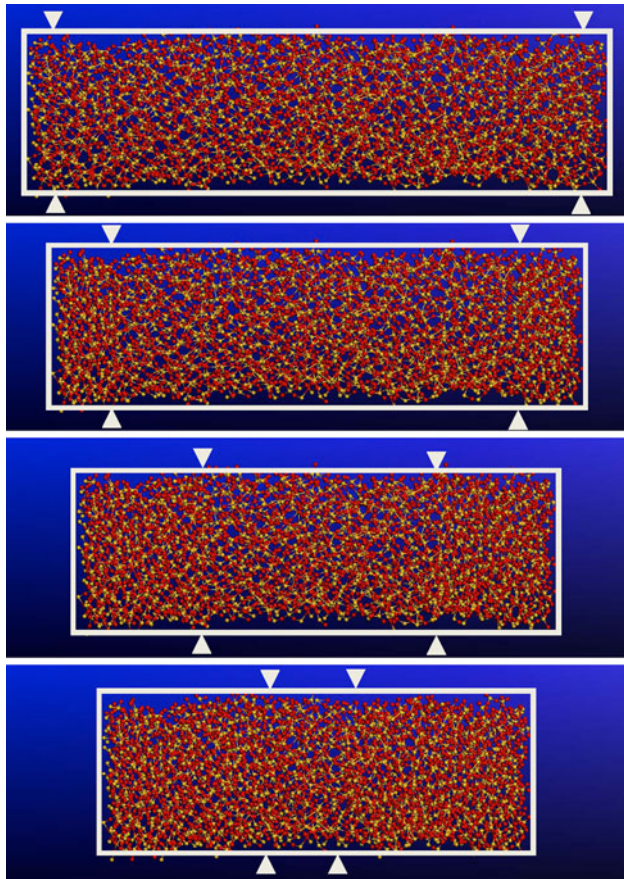


Fig. 6 Temporal evolution of the molecular level material microstructure accompanying generation and propagation of a pair of planar shocks in fused silica. Arrows denote the position of the shock front mid-plane

simulation (i.e., post-shock-wave generation) times are plotted against the Lagrangian-bin mid-plane x -location. The results displayed in Fig. 7(b) are obtained under identical simulation conditions except for the rate of axial contraction of the computational cell (3000 m/s in Fig. 7(a) and 2400 m/s in Fig. 7(b)).

A brief examination of the results displayed in Fig. 7(a) and (b) reveals that

- (a) two shocks are generated (only the right-propagating shock is shown, though) at the computational cell faces normal to the x -direction. These shocks subsequently propagate towards the computational-cell center;
- (b) following a brief transient period, the (right-propagating) shock appears to become steady (i.e., within a reference frame which is attached to, and moves with, the shock-wave front, the wave front is nearly time-invariant);
- (c) the particle velocity and the shock speed increase while shock-wave width decreases with an increase in the computational-cell contraction rate. It should be noted that the curves displayed in Fig. 7(a) and (b) are labeled using the associated post-shock generation times in femtoseconds.

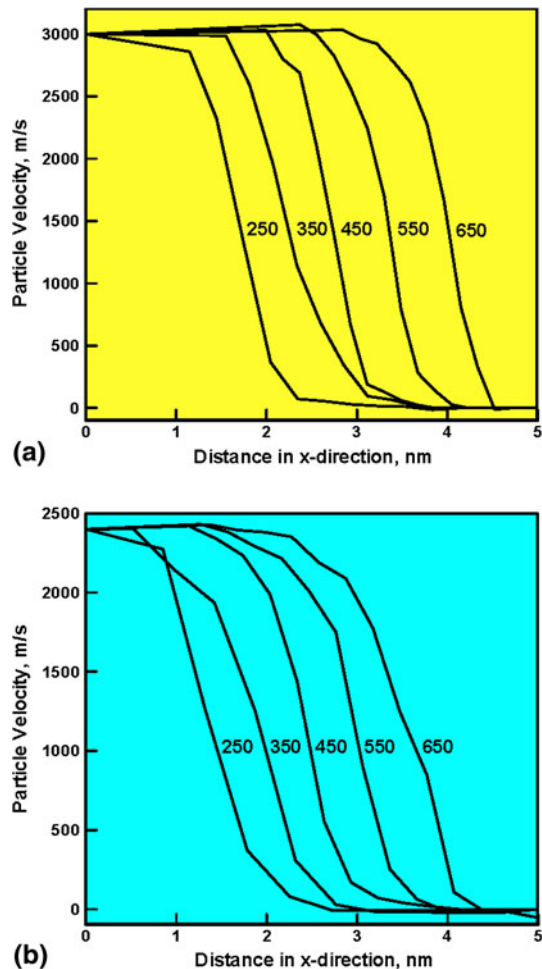


Fig. 7 Temporal evolution of the particle velocity associated with the propagation of a right-propagating planar shock in fused silica under the imposed computational cell contraction rate of (a) 3000 m/s and (b) 2400 m/s. Curve labels denote the associated post shock-generation time in femtoseconds

It should also be noted that no (artificial viscous-damping based) thermostat was used in the present non-equilibrium molecular-dynamics simulations. Thus, the observed steady-shock-wave profile is a natural consequence of a balance between the continuous supply of energy to the system (through the continuous computational cell axial contraction) and the attendant bond/microstructure-altering atomic motions in the continuously enlarged upstream material region swept by the shock. Further examination of the results displayed in Fig. 7(a) and (b) reveals that in the shockstrength range examined, the observed shock width is quite small (ca. 2-3 nm) and that it decreases with an increase in shock strength. This finding suggests that the dominant energy dissipation processes captured by the molecular-level simulations of shock generation/propagation within fused silica are quite weak. As will be shown later, these processes involve changes in the fused silica atomic coordination and in the size of the smallest Si-O rings. In other words, the known viscous dissipation processes with characteristic times at the microsecond time scale are not active in (captured by) the present simulations. Based on the fundamental analysis of propagation of the structured longitudinal planar shocks (Ref 35), this fact, in general, only affects the width of the shock profile but not the values of the as-shocked material state variables.

4.2.3 Non-Equilibrium Shock Hugoniot Relations. The results like the ones displayed in Fig. 7(a) and (b) were utilized to determine a functional relationship between the (Lagrangian) shock speed, U_s , and the particle velocity, u_p . The outcome of this procedure is displayed in Fig. 8. The U_s versus u_p relation like the one displayed in Fig. 8 is generally considered as one of the shock Hugoniot relations. Since, as discussed earlier, the Hugoniot is geometrically a hyper-line in a multi-dimensional stress/pressure, energy density, mass density (or specific volume), temperature, particle velocity, shock-speed etc. space. The U_s versus u_p (Fig. 8) and the negative axial-stress versus specific volume (Fig. 5) relations are simply the particular planar (two-dimensional) projections of the Hugoniot. The U_s versus u_p Hugoniot data displayed in Fig. 8 are fitted to a linear relationship in the form $U_s = c_0 + su_p$, and the following values of the two coefficients are obtained as $c_0 = 2560$ m/s and $s = 1.182$.

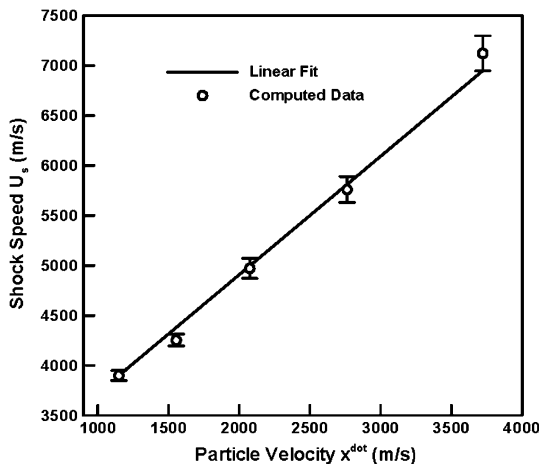


Fig. 8 Shock-speed vs. particle-velocity Hugoniot data (based on the present results like the ones displayed in Fig. 7(a) and (b)) and the corresponding linear fit to the data

The other commonly used planar shock Hugoniot relations include negative axial-stress versus mass-density, ρ ; (mass-based) internal energy density, E , versus ρ (or v); $-t_{11}$ versus u_p , and temperature T versus ρ (or v). Following our prior studies (Ref 9, 21), an attempt was made to determine these relations using two distinct methods:

(a) A method based on the Lagrangian form of the three jump equations defined as

$$\rho^- U_s = \rho^+ (U_s - u_p) \quad (\text{Eq } 4)$$

$$t_{11}^- + \rho^- U_s^2 = t_{11}^+ + \rho^+ (U_s - u_p)^2 \quad (\text{Eq } 5)$$

$$e^- + \frac{t_{11}^-}{\rho^-} + 0.5 U_s^2 = e^+ + \frac{t_{11}^+}{\rho^+} + 0.5 (U_s - u_p)^2 \quad (\text{Eq } 6)$$

The above equations relate the known downstream material states (denoted by a superscript “-”) and the unknown upstream material states (denoted by a superscript “+”) associated with the shock of a given strength (as quantified by the shock speed or the downstream-to-upstream particle velocity jump). These equations are next combined with the previously determined U_s versus u_p relation and the prescribed (shock-strength defining quantity) U_s or u_p to solve for the unknown upstream/as-shocked material states. It should be noted that this method enables determination of only material mechanical state variables (t_{11} , E , $v(=1/\rho)$, U_s and u_p). To obtain temperature-based Hugoniot relations, the procedure described recently in Ref 36 was employed. This procedure involves the following steps: (i) the (differential) statement of the combined first and second laws of thermodynamics is equated to the differential form of the Rankine-Hugoniot equation; (ii) the term representing the rate of change of mass-based entropy density with the specific volume appearing in the resulting equation is eliminated using the expression for the total derivative of temperature and the Maxwell equation based thermodynamic relations; and (iii) the resulting differential equation which now contains additional material parameters (the constant-volume specific heat and the Gruneisen Gamma) and the stress/pressure Hugoniot relation is integrated numerically between the initial and the final material states to obtain the temperature corresponding to the given shock strength; and (b) Thermodynamic averages of the as-shocked material in the shock are used to calculate the temperature (as well as the remaining material state variables like stress/pressure, specific-volume/density, mass-based energy density, etc.). The necessary data were collected using non-Lagrangian bins. These bins were attached to (and moved with) the steady-shock front and hence, in contrast to the Lagrangian bins, collected the information about the atoms (temporarily) residing in a given segment of the steady-shock profile rather than the information about a fixed set of atoms. Also, since the main role of these bins was to collect the data in the upstream material, they were placed only in the regions behind the shock. This procedure was found to be quite work intensive and to yield widely scattered results. To overcome these shortcomings, an attempt was made to carry out NVE (E is the total energy of the computational cell) molecular-dynamics simulations (over an extended time period) on the material extracted from the upstream region and placed into its own periodic cell. Unfortunately, this attempt was not very successful since prolonged molecular level simulations of the “shocked material” were associated with extensive material relaxation so that

the material molecular structure did not any longer correspond to the as-shocked material state. Consequently, the shock-Hugoniot results obtained using this procedure are deemed unreliable and are not shown and not used in the remainder of this article.

The results of the method (a), based on the use of the shock-jump equations, are depicted in Fig. 9(a)-(d). These four figures show the $-t_{11}$ versus ρ , E versus ρ , $-t_{11}$ versus u_p , and T versus ρ Hugoniot relations, respectively. In addition, the non-equilibrium $-t_{11}$ versus v/v_0 Hugoniot relation is depicted in Fig. 5 and compared with its equilibrium computational and experimental counterparts. It should be noted that only the non-equilibrium molecular-dynamics results associated with the strong- and moderate-shock regimes are displayed in Fig. 5. The reason for this is that, under weak-shock conditions, the results did not show the formation of a well-defined shock. This finding is consistent with the experimental Hugoniot curve in Fig. 5 which, in the weak-shock régime, is concave downward, suggesting an abnormal (i.e., a non-shock-supporting) behavior of fused silica under compressive loading. In other words, in the weak-shock regime, compressive loading tends to produce spreading finite-amplitude waves rather than shocks. Examination of Fig. 5 reveals that the non-equilibrium computed Hugoniot data are in substantially better agreement with their

experimental counterparts than are the equilibrium computed results.

The Hugoniot relations displayed in Fig. 5 and Fig. 9(a)-(d) are typically used within a continuum-level computational analysis of shock-wave generation/ propagation in two ways:

- (a) They are directly used in the analysis of planar longitudinal shock-wave propagation under uniaxial strain conditions (Ref 37) and
- (b) Alternatively, they can be used to derive a continuum-level material model which is consistent with the material mechanical response under high-rate, large-strain, high-pressure conditions. Such a model is subsequently used in general three-dimensional, nonlinear dynamics computational analyses (Ref 38, 39).

4.2.4 Shock-Induced Material Microstructure-Evolution. The results presented and discussed in the previous sections clearly revealed the formation and propagation of planar shocks in fused silica and enabled formulation of the appropriate shock-Hugoniot relations. In the present section, a more detailed investigation of the molecular-level material microstructure, in the wake of a propagating planar shock, is carried out.

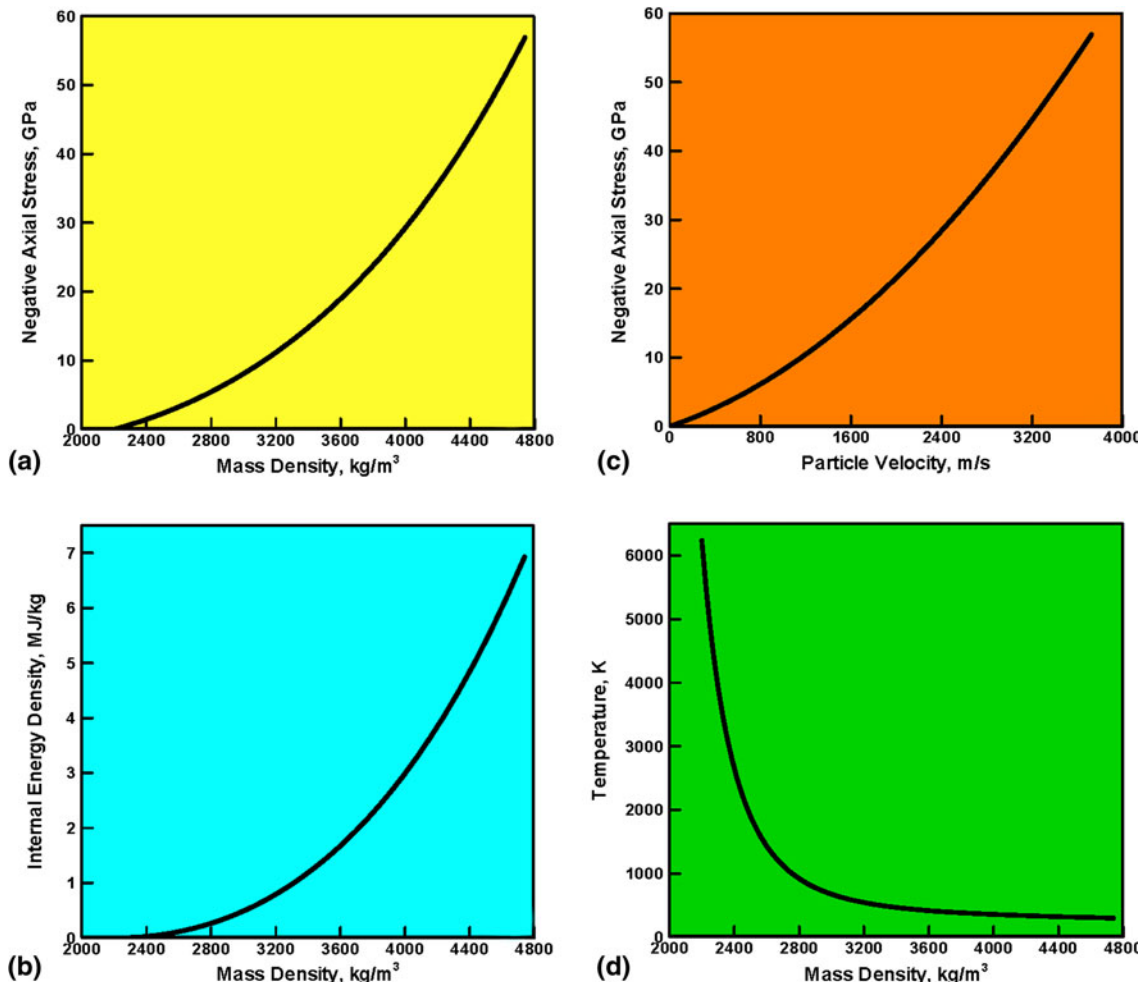


Fig. 9 (a) Negative axial-stress vs. mass-density; (b) internal energy density vs. mass-density, (c) negative axial stress vs. particle velocity, and (d) temperature vs. mass-density Hugoniot relations for fused silica obtained using non-equilibrium molecular-dynamics calculations

At the onset, it should be noted that, the absence of a crystal structure in fused silica makes the analysis of material microstructure and its evolution a formidable task. That is, the presence of a crystal lattice (as is the case in single-crystal solids) studied earlier (Ref 40, 41) makes the analysis of shock-loading induced changes and the associated deformation processes in the material microstructure more tractable. Fused silica, on the other hand, is an amorphous material in both its initial and its as-shocked state. To quantify the extent of shock-induced changes in the microstructure of fused silica, the following microstructural parameters were tracked: (a) the random network X parameter, defined earlier. The R parameter ($=2.0$) was not monitored since its value is controlled by glass-chemistry and not by the material microstructure. The Y -parameter was not tracked either since in fused silica the $X + Y$ sum is equal to 4.0; (b) the size-distribution of the smallest Si-O rings; (c) the Si-atom average coordination number (i.e., bonding structure); and (d) the radial distribution function.

Changes in X Parameter. Shock-induced changes in the random-network X parameter are found to be the result of a competition between Si-O bond breaking processes (increase the average number of non-bridging oxygens per un-shocked material polyhedron) and the ones which lead to an increase in Si-atom coordination number (decrease the X -parameter value). The results obtained in the present study show that the instances of Si-atom coordination number increase greatly out-number the ones associated with Si-O bond-breaking. Consequently, the value of the X parameter has been found to decrease by 5–10% (with the largest percent changes observed under the strongest-shock loading conditions).

Size Distribution of the Smallest Si-O Rings. It is customary to monitor changes in the size distribution of the smallest Si-O rings and use the same as an evidence for the attendant shock-induced microstructural changes. However, one should exercise caution at this juncture. It should be first noted that the crystobalite allotropic modifications of SiO_2 contain only the so-called six-membered rings (i.e., rings containing six silicon and six oxygen atoms). In quartz, on the other hand, one finds both six member and eight member Si-O rings. In both cases, the total number of the smallest rings associated with each Si atom is six, and silicon atoms are four-fold coordinated. Intuitively, one would expect that a larger fraction of smaller rings in a given allotropic modification would yield a material with closer packing and, thus, a higher density. However, this is not the case considered for this study since the density of crystobalite is 2.17 g/cm^3 while that for quartz is 2.64 g/cm^3 . The structure of the six-membered rings in crystobalite and quartz are displayed in Fig. 10(a) and (b). Examination of Fig. 10(a) and (b) reveals that the atomic structures of the six-membered rings in the two SiO_2 allotropes are quite different and that these rings in quartz occupy less space than the ones in crystobalite. Furthermore, in stishovite in which silicon atoms have six-fold coordination, one finds the two- and three-membered Si-O rings and the density is 4.29 g/cm^3 . This brief analysis suggests that there is no simple correlation between the size of the smallest Si-O rings (as measured by the number of Si and O atoms in the rings) and the fused silica material density or its microstructure. Instead, the information regarding the size, topology, and distribution of the smallest rings should be combined with the silicon atom coordination data.

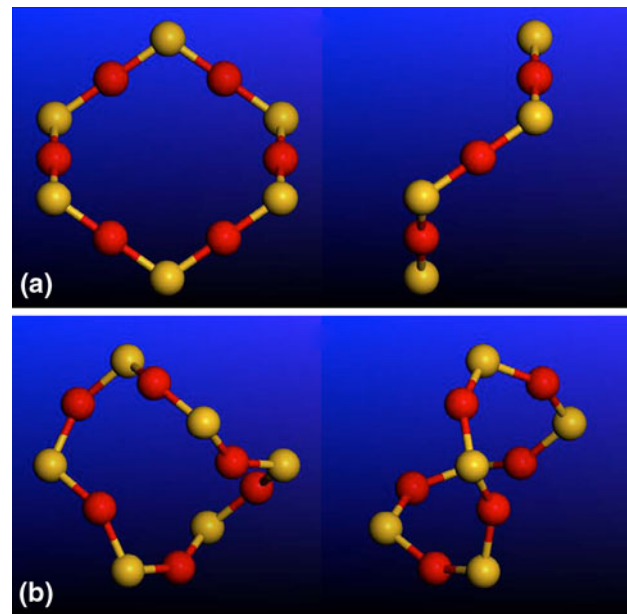


Fig. 10 Two views of the atomic structure of six-membered Si-O rings in (a) crystobalite and (b) quartz

To quantify the size-distribution of the smallest Si-O rings in both the initial and the as-shocked fused-silica states, a computational method was developed as part of the present study. This method solves the class of so-called shortest-path problems and is a simple modification of the Dijkstra's algorithm (Ref 42). The main modifications in this algorithm are associated with the fact that, in the present case, the starting point and the destination point of the path are identical. The smallest-ring size-distribution results for the initial and two representative as-shocked material states are displayed in Fig. 11(a) and (b), respectively.

Since, the as-shocked results obtained under different loading conditions, Fig. 11(b), are mutually similar and substantially different than the ones associated with the initial state, Fig. 11(a), one can conclude that the material undergoes detectable microstructural changes during shock loading. This finding was further supported by the observations that, while the six-membered Si-O rings in the fused-silica initial state were similar to those found in crystobalite, Fig. 10(a), the six-membered Si-O rings observed in the as-shocked material state resembled more to the ones found in quartz, Fig. 10(b). Also, no five-membered rings were found in the initial states while the same were observed in the as-shocked state. An example of the five-membered Si-O ring found in fused-silica as-shocked state is displayed in Fig. 12(a). For clarity, the silicon and oxygen atoms associated with the five-membered ring are colored white and green, respectively, while the remaining Si and O atoms are colored yellow and red, respectively.

Si-Atom Average Coordination Number. Examination of the as-shocked material microstructure of fused silica revealed that the Si-atom average coordination number increases from its initial value of 4.0–4.06. An example of the shock-loading-induced increase in Si-atom coordination number is depicted in Fig. 12(b). In this figure, a five-fold-coordinated Si-atom (white) is displayed along with the associated five oxygen atoms (green). The remaining Si and O atoms are displayed as

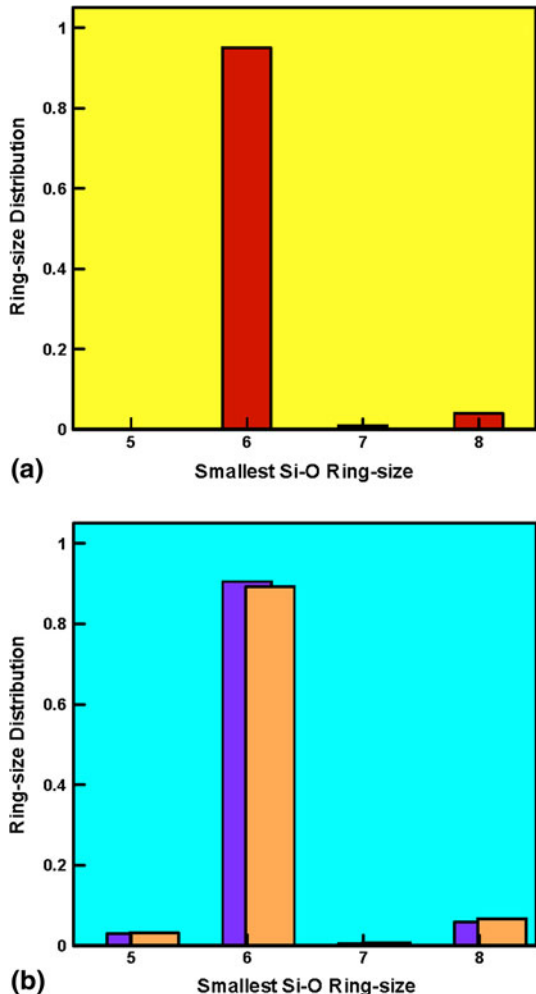


Fig. 11 Size distribution function for the smallest Si-O rings in the fused silica: (a) initial state and (b) two as-shocked states

yellow and red, respectively. The forgoing finding regarding an increase in the Si-atom coordination is an indication of the transition of fused silica to a “stishovite-like” state, an energetically favored state at high shock-induced stresses. This finding is consistent with the experimental observation of Alexander et al. (Ref 43) who reported the formation of stishovite-like domains in various silica-based glasses after being subjected to shock loading in excess of 30 GPa.

Radial Distribution Function. The last microstructure-characterizing quantity covered in the present analysis is the radial distribution function. In Fig. 4(c), the Si-Si, Si-O, and O-O partial radial distribution functions are displayed for a typical as-shocked material state. Comparison of the results displayed in Fig. 4(a) and (c) provides additional evidence that shock loading gives rise to the changes in fused-silica material microstructure.

4.3 Final Remarks

Previous non-equilibrium molecular-dynamics simulations of shock-wave propagation in single-crystalline solids (Ref 40, 41) established that energy dissipation accompanying shock propagation is the result of inelastic deformation (permanent

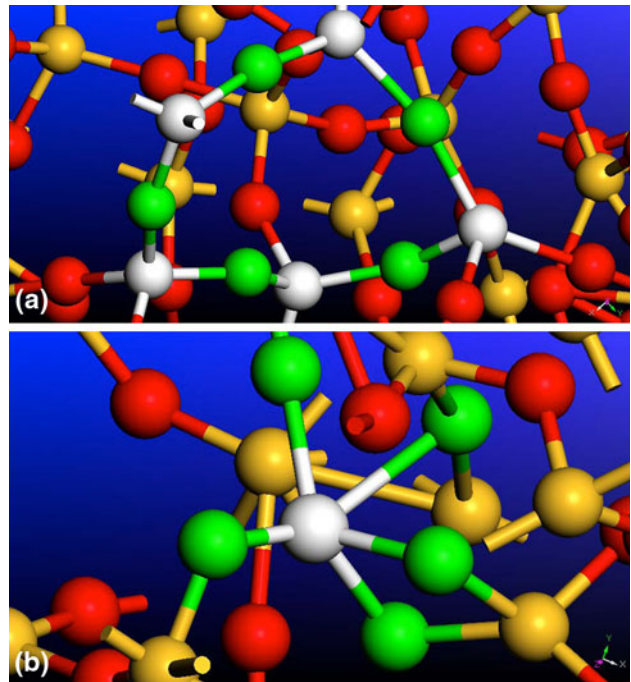


Fig. 12 Examples of (a) a five-membered Si-O ring and (b) five-fold coordinated Si-atom in as-shocked fused-silica material state. The silicon atom in question is colored white (the remaining Si atoms are shown as yellow), and the associated O-atoms are shown as green (the remaining O-atoms are shown as red) (Color figure online)

slippage of crystal planes and the formation of crystal defects) and phase-transformation processes and not a result of (velocity-dependent) viscous dissipation (as is the case for shocks in fluids). The present computational results obtained in fused silica suggest that this may be also true in the case of amorphous solids. This finding provides a possible explanation for the fact that the axial-stress versus specific volume equilibrium and non-equilibrium Hugoniots differ significantly under moderate and strong shock regimes and the non-equilibrium Hugoniot is in better agreement with the experimental one. In other words, the equilibrium Hugoniot was derived under the assumption that the material microstructure does not change under shock loading. When such changes take place, the Hugoniot states no-longer lie on the initial equation-of-state surface but rather on a surface(s) associated with the transformed material state. Since the energy levels associated with the transformed-material equation-of-state surface are generally higher when compared to their initial-material counterparts, the corresponding axial-stress values are expected to be higher. This was indeed confirmed by the non-equilibrium molecular-dynamics results displayed in Fig. 5.

In the present study, molecular-level computational methods and tools are employed to investigate shock-wave generation and propagation phenomena in fused silica. However, it is not the objective here to suggest that shock-wave molecular-level simulations should replace the corresponding hydrodynamic/continuum-level computations. In fact, the latter are generally preferred in the studies dealing with real-world technical systems (e.g., blast impact of vehicle windshields). On the other hand, molecular-level simulations appear to be highly benefi-

cial in determining the shock-Hugoniot relations and in identifying key microstructure-altering and deformation processes accompanying shock propagation. As pointed out earlier, the knowledge of the shock Hugoniot relations and the associated phase-transformation/deformation processes can be used to derive physically based continuum-level material models which are used in the aforementioned hydrodynamic analyses.

5. Summary and Conclusions

Based on the results obtained in the present study, the following summary remarks and main conclusions can be drawn:

1. Equilibrium and non-equilibrium molecular-dynamics computational analyses are employed to study the propagation of planar longitudinal shocks in fused silica, a material commonly used in transparent armor applications.
2. To create molecular-level shocks, a computational procedure based on continuously contracting computational cell is used. This procedure does not require the use of a viscous-dissipation-based thermostat to form a steady shock wave.
3. By properly post-processing the computational results pertaining to the atomic positions, velocities, and interaction forces, appropriate shock Hugoniot relations are derived. These relations define the locus of stress, energy density, mass density, temperature, and particle velocity in the as-shocked states of fused silica.
4. Detailed examination of the molecular-level microstructure in the as-shocked state of fused silica is carried out to identify the nature of the microstructure-altering and deformation processes responsible for energy dissipation accompanying shock-wave propagation. This examination identified significant and shock-strength-dependent changes in the silicon atom coordination on the structure of the Si-O random-network connectivity. In particular, a substantially larger number of five-fold coordinated Si atoms has been found in the as-shocked state relative to that found in the pre-shocked fused-silica initial state. Also, smaller Si-O rings, not found in the initial state, have been observed in the fused silica with as-shocked state. It has been subsequently shown that these microstructural changes give rise to a deviation of the equation-of-state surface for the as-shocked material compared with the initial material. Consequently, higher stress-levels are attained in the as-shocked material than the ones which are predicted by an analysis based on the equilibrium equation-of-state.

Acknowledgments

The research material presented in this article is based on study supported by the U.S. Army/Clemson University Cooperative Agreements W911NF-04-2-0024 and W911NF-06-2-0042 and by the Army Research Office (ARO) research contract entitled “Multi-length Scale Material Model Development for Armor-grade Composites,” Contract Number W911NF-09-1-0513.

Appendix A: Nose-Hoover Thermostat (Ref 25)

The simulated-annealing computational procedure described in section 3.1 employed *NVT* molecular-dynamics simulations in which temperature was controlled using the Nose-Hoover thermostat (Ref 25).

In this section, a brief description is provided of this temperature-control algorithm. Within this algorithm, the real (constant-temperature) molecular-level material system characterized by the particle coordinates q'_i and linear momenta p'_i ($i = 1, 2, \dots, 3 N$), as well as by a fixed temperature T is replaced with an extended (constant-energy) system containing modified degrees of freedom $q_i = q'_i$, $p_i = \frac{p'_i}{s}$ and two additional degrees of freedom s (a dimensionless coordinate) and p_s (the conjugate linear momentum). The extended system Hamiltonian (the total energy) is then defined as

$$H = \sum_i p_i^2 / 2m_i s^2 + \varphi(q_i) + p_s^2 / 2Q + gkT \ln s \quad (\text{Eq A.1})$$

while the associated equations of motion are defined as

$$\frac{dq_i}{dt} = \frac{\partial H}{\partial p_i} = \frac{p_i}{m_i} s^2 \quad (\text{Eq A.2})$$

$$\frac{dp_i}{dt} = -\frac{\partial H}{\partial q_i} - \frac{\partial \varphi}{\partial q_i} \quad (\text{Eq A.3})$$

$$\frac{ds}{dt} = \frac{\partial H}{\partial p_s} = \frac{p_s}{Q} \quad (\text{Eq A.4})$$

$$\frac{dp_s}{dt} = -\frac{\partial H}{\partial s} = \frac{(\sum_i p_i^2 / 2m_i s^2 - gkT)}{s} \quad (\text{Eq A.5})$$

where Q is a mass term, associated with the added degrees of freedom, $\varphi(q_i)$ is the real-system force-field potential, g (=3 N), and k is the Boltzmann’s constant. The temperature control is then carried out by integrating the extended system in time and projecting the (computed) extended (*NVE* canonical-ensemble related) system trajectory data onto the real (*NVT* microcanonical ensemble related) system.

Appendix B: Berendsen Barostat (Ref 31)

Within this barostat, pressure is controlled by scaling the particle coordinates and the computational-cell edge lengths while maintaining the shape of the computational cell. This, in a way, is similar to coupling the system to a constant-pressure environment. The strength of the coupling is controlled by the user-specified coupling-intensity parameter γ and a relaxation/response time, τ . During each time step of duration Δt , the particle-coordinate/cell edge-length scaling factor, μ , is computed as

$$\mu = \left(1 + \frac{\Delta t}{\tau} \gamma (P - P_0) \right)^{\frac{1}{3}} \quad (\text{Eq B.1})$$

where P is the instantaneous pressure, and P_0 is the target pressure. The instantaneous pressure is obtained from the virial theorem (Ref 44) as

$$P = \frac{2}{3V}(K + W) \quad (\text{Eq B.2})$$

where K and V are respectively the instantaneous kinetic energy of the particles residing within and the volume of the computational cell, and W is the instantaneous virial defined as a scalar product of two vectors, one defined by the instantaneous coordinates of all particles in the cell, and the other by the corresponding force components.

References

1. E. Strassburger, P. Patel, W. McCauley, and D.W. Templeton, Visualization of Wave Propagation and Impact Damage in a Polycrystalline Transparent Ceramic-AlON, *Proceedings of the 22nd International Symposium on Ballistics*, November 2005 (Vancouver, Canada)
2. Army Materials Research: Transforming Land Combat Through New Technologies, *AMPTIAC Q.*, 2004, **8**(4)
3. G.A. Gazonas, J.W. McCauley, I.G. Batyrev, R.C. Becker, P. Patel, B.M. Rice, and N.S. Weingarten, "Multiscale Modeling of Non-crystalline Ceramics (Glass)," ARL Technical Report, ARL Aberdeen Proving Ground, January 2011
4. B. Moran, L.A. Glenn, and A. Kusubov, Jet Penetration in Glass, *J. Phys. IV*, 1991, **1**(C3), p 147–154
5. M. Grujicic, B. Pandurangan, N. Coutris, B.A. Cheeseman, C. Fountzoulas, P. Patel, and E. Strassburger, A Ballistic Material Model for Starphire®, A Soda-Lime Transparent Armor Glass, *Mater. Sci. Eng. A*, 2008, **492**(1), p 397–411
6. M. Grujicic, B. Pandurangan, W.C. Bell, N. Coutris, B.A. Cheeseman, C. Fountzoulas, and P. Patel, An Improved Mechanical Material Model for Ballistic Soda-Lime Glass, *J. Mater. Eng. Perform.*, 2009, **18**(8), p 1012–1028
7. M. Grujicic, B. Pandurangan, N. Coutris, B.A. Cheeseman, C. Fountzoulas, and P. Patel, A Simple Ballistic Material Model for Soda-Lime Glass, *Int. J. Impact Eng.*, 2009, **36**, p 386–401
8. M. Grujicic, W.C. Bell, P.S. Glomski, B. Pandurangan, B.A. Cheeseman, C. Fountzoulas, P. Patel, D.W. Templeton, and K.D. Bishnoi, Multi-Length Scale Modeling of High-Pressure Induced Phase Transformations in Soda-Lime Glass and Their Effect on Blast/Ballistic-Impact Mitigation, *J. Mater. Eng. Perform.*, 2010. doi:[10.1007/s11665-010-9774-2](https://doi.org/10.1007/s11665-010-9774-2)
9. M. Grujicic, B. Pandurangan, W.C. Bell, B.A. Cheeseman, P. Patel, and G.A. Gazonas, Molecular-Level Analysis of Shock-Wave Physics and Derivation of the Hugoniot Relations for Soda-Lime Glass, *J. Mater. Sci.*, 2011. doi:[10.1007/s10853-011-5691-5](https://doi.org/10.1007/s10853-011-5691-5)
10. M. Grujicic, B. Pandurangan, and N. Coutris, A Computational Investigation of the Multi-Hit Ballistic-Protection Performance of Laminated Transparent-armor Systems, *J. Mater. Eng. Perform.*, 2011. doi:[10.1007/s11665-011-0004-3](https://doi.org/10.1007/s11665-011-0004-3)
11. L.V. Woodcock, C.A. Angell, and P. Cheeseman, Molecular Dynamics Studies of the Vitreous State: Simple Ionic Systems and Silica, *J. Chem. Phys.*, 1976, **65**, p 1565–1577
12. R.G.D. Valle and E. Venuti, High-Pressure Densification of Silica Glass: A Molecular-Dynamics Simulation, *Phys. Rev. B*, 1996, **54**(6), p 3809–3816
13. K. Trachenko and M.T. Dove, Densification of Silica Glass Under Pressure, *J. Phys. Condens. Matter*, 2002, **14**, p 7449–7459
14. Y. Liang, C.R. Miranda, and S. Scandolo, Mechanical Strength and Coordinate Defects in Compressed Silica Glass: Molecular Dynamics Simulations, *Phys. Rev. B*, 2007, **75**, p 024205
15. B. Nghiem, PhD Thesis, University of Paris 6, France, 1998
16. C. Denoual and F. Hild, Dynamic Fragmentation of Brittle Solids: A Multi-Scale Model, *Eur. J. Mech. Solids A*, 2002, **21**, p 105–120
17. M. Yazdchi, S. Valliappan, and W. Zhang, A Continuum Model for Dynamic Damage Evolution of Anisotropic Brittle Materials, *Int. J. Numer. Methods Eng.*, 1996, **39**, p 1555–1583
18. F. Hild, C. Denoual, P. Forquin, and X. Brajer, On the Probabilistic and Deterministic Transition Involved in a Fragmentation Process of Brittle Materials, *Comput. Struct.*, 2003, **81**, p 1241–1253
19. T.J. Holmquist, D.W. Templeton, and K.D. Bishnoi, Constitutive Modeling of Aluminum Nitride for Large Strain High-Strain Rate, and High-Pressure Applications, *Int. J. Impact Eng.*, 2001, **25**, p 211–231
20. G.T. Camacho and M. Ortiz, Computational Modeling of Impact Damage in Brittle Materials, *Int. J. Solids Struct.*, 1996, **33**(20–22), p 2899–2938
21. M. Grujicic, B. Pandurangan, W.C. Bell, B.A. Cheeseman, C.F. Yen, and C.L. Randow, Molecular-Level Simulations of Shock Generation and Propagation in Polyurea, *Mater. Sci. Eng. A*, 2011, **528**(10–11), p 3799–3808
22. W.D. Kingery, H.K. Bowen, and D.R. Uhlmann, *Introduction to Ceramics*, 2nd ed., John Wiley & Sons, New York, 1976, p 91–124
23. <http://www.accelrys.com/mstudio/msmodeling/visualiser.html>
24. Y.H. Tu, J. Tersoff, G. Grinstein, and D. Vanderbilt, Properties of a Continuous-Random-Network Model for Amorphous Systems, *Phys. Rev. Lett.*, 1998, **81**(22), p 4899–4902
25. S. Nose, Constant Temperature Molecular Dynamics Methods, *Prog. Theor. Phys. Suppl.*, 1991, **103**, p 1–46
26. H. Sun, COMPASS: An Ab Initio Force-Field Optimized for Condensed-Phase Applications Overview with Details on Alkane and Benzene Compounds, *J. Phys. Chem. B*, 1998, **102**, p 7338–7364
27. H. Sun, P. Ren, and J.R. Fried, The COMPASS Force Field: Parameterization and Validation for Phosphazenes, *Comput. Theor. Polym. Sci.*, 1998, **8**(1/2), p 229–246
28. M. Grujicic, Y.P. Sun, and K.L. Koudela, The Effect of Covalent Functionalization of Carbon Nanotube Reinforcements on the Atomic-Level Mechanical Properties of Poly-Vinyl-Ester-Epoxy, *Appl. Surf. Sci.*, 2007, **253**, p 3009
29. <http://www.accelrys.com/mstudio/msmodeling/discover.html>
30. A.V. Amirkhizi, J. Isaacs, J. McGee, and S. Namet-Nasser, An Experimentally Based Viscoelastic Constitutive Model for Polyurea Including Pressure and Temperature Effects, *Philos. Mag.*, 2006, **86**(36), p 5847–5866
31. H.J.C. Berendsen, J.P.M. Postma, W.F. van Gunsteren, A. DiNola, and J.R. Haak, Molecular Dynamics with Coupling to an External Bath, *J. Chem. Phys.*, 1984, **81**(8), p 3684–3690
32. A. Tilcock, N.H. de Leeuw, and A.N. Cormack, Shell-Model Molecular Dynamics Calculations of Modified Silicate Glasses, *Phys. Rev. B*, 2006, **73**, p 10
33. J.J. Erpenbeck, Molecular-Dynamics of Detonation 1: Equation of State and Hugoniot Curve for a Simple Reactive Fluid, *Phys. Rev. A*, 1992, **46**(10), p 6406–6416
34. S.P. Marsh, Ed., *LASL Shock Hugoniot Data*, University of California Press, Berkeley, CA, 1980
35. L. Davison, *Fundamentals of Shock Wave Propagation in Solids*, Springer-Verlag, Berlin, Heidelberg, Germany, 2008
36. M. Grujicic, B. Pandurangan, W.C. Bell, and S. Bagheri, Shock-Wave Attenuation and Energy-Dissipation Potential of Granular Materials, *J. Mater. Eng. Perform.*, 2011. doi:[10.1007/s11665-011-9954-8](https://doi.org/10.1007/s11665-011-9954-8)
37. M. Grujicic, W.C. Bell, B. Pandurangan, and T. He, Blast-Wave Impact-Mitigation Capability of Polyurea When Used as Helmet Suspension-Pad Material, *J. Mater. Des.*, 2010, **31**(9), p 4050–4065
38. M. Grujicic, G. Arakere, and T. He, Material-Modeling and Structural-Mechanics Aspects of the Traumatic Brain Injury Problem, *Multidiscip. Model. Mater. Struct.*, 2010, **6**(3), p 335–363
39. M. Grujicic, W.C. Bell, B. Pandurangan, and P.S. Glomski, Fluid/Structure Interaction Computational Investigation of Blast-Wave Mitigation Efficacy of the Advanced Combat Helmet, *J. Mater. Eng. Perform.*, 2010. doi:[10.1007/s11665-010-9724-z](https://doi.org/10.1007/s11665-010-9724-z)
40. B.L. Holian and G.K. Straub, Molecular Dynamics of Shock Waves in Three-Dimensional Solids: Transition from Nonsteady to Steady Waves in Perfect Crystals and Implications for the Rankine-Hugoniot Conditions, *Phys. Rev. Lett.*, 1958, **43**, p 1979
41. B.L. Holian, W.G. Hoover, B. Moran, and G.K. Straub, Shock-Wave Structure via Non-Equilibrium Molecular Dynamics and Navier-Stokes Continuum Mechanics, *Phys. Rev. A*, 1980, **22**, p 2498
42. E.W. Dijkstra, A Note on Two Problems in Connexion with Graphs, *Numer. Math.*, 1959, **1**, p 269–271
43. C.S. Alexander, L.C. Chhabildas, W.D. Reinhart, and D.W. Templeton, Changes to the Shock Response of Fused Quartz due to Glass Modification, *Int. J. Impact Eng.*, 2008, **35**, p 1376–1385
44. R.J.E. Clausius, On a Mechanical Theorem Applicable to Heat, *Philos. Mag. Ser. 4*, 1870, **4**(40), p 122–127